Available online at www.sciencedirect.com

ScienceDirect

Journal of Catalysis 252 (2007) 190–204

JOURNAL OF CATALYSIS

www.elsevier.com/locate/jcat

Beneficial effects of the use of a nickel membrane reactor for the dry reforming of methane: Comparison with thermodynamic predictions

Stéphane Haag, Michel Burgard, Barbara Ernst *

Laboratoire des Procédés de Séparation (LPS), IPHC-DSA, ULP, CNRS 7178, Ecole Européenne de Chimie, Polymères et Matériaux (ECPM),
25 rue Becquerel, 67087 Strasbourg Cedex 2, France

Received 22 May 2007; revised 25 September 2007; accepted 27 September 2007

Abstract

The development of a nickel composite membrane with acceptable hydrogen permselectivity at high temperature in a membrane reactor for the highly endothermic dry reforming of methane reaction was the purpose of this work. A thin, catalytically inactive nickel layer, deposited by electroless plating on asymmetric porous alumina, behaved simply as a selective hydrogen extractor, shifting the equilibrium in the direction of a higher hydrogen production and methane conversion. The main advantage of such a nickel/ceramic membrane reactor is the elimination or limitation of the side reverse water gas shift reaction. For a Ni/Al_2O_3 catalyst, containing free Ni particles, normally sensitive to coking, the use of the membrane reactor allowed an important reduction of carbon deposition (nanotubes) due to restriction of the Boudouard reaction. For a $Ni–Co/Al_2O_3$ catalyst, where the metallic nickel phase was stabilized by the alumina, the selective removal of the hydrogen significantly enhanced both methane conversion (+67% at 450 °C, +22% at 500 °C and +18% at 550 °C) and hydrogen production (+42% at 450 °C, +32% at 500 °C and +22% at 550 °C) compared to the results obtained for a packed-bed reactor. The hydrogen selectivity during the catalytic tests at 550 °C, maintained with constant separation factors (7 for H_2/CH_4, 8 for H_2/CO and 10 for H_2/CO_2), higher than Knudsen values, attested to the high thermal stability of the nickel composite membrane.

Keywords: Nickel; Membrane reactor; Hydrogen permselectivity; Dry methane reforming; Thermodynamic prediction

1. Introduction

Inorganic membranes for gas separation have been widely studied over the last two decades, but their possible use in a high-temperature membrane reactor for endothermic reactions remains a challenge, especially for hydrogen extraction. Methane reforming, in particular, requires high-quality membranes that should exhibit high thermal stability and chemical inertness. Most studies of the partial oxidation of methane in membrane reactors have focused on vaporeforming [1–7], which is a less endothermic reaction compared with the methane reforming with carbon dioxide. Despite the appeal of transformation of two greenhouse gases into syngas (a mixture of hydrogen and carbon monoxide that can be used as raw material in many chemical processes), only recently has membrane technology been used for the dry reforming of methane [8–18]. For this highly endothermic reaction ($CH_4 + CO_2 \leftrightarrow 2CO + 2H_2$; $\Delta H^\circ_{\text{reaction}}(298\ \text{K}) = 247.3\ \text{kJ/mol}$), the objective is to enhance reactant conversion by selectively removing the produced hydrogen, thus shifting the reaction equilibrium in the direction of syngas production. Known membranes for the dry reforming of methane are either dense metallic membranes composed of palladium or palladium and its Ag alloys [8,10–12] or porous membranes (mesoporous ceramic [13], Vycor glass and nanosil [14–16], or zeolites [9]). In most cases, the membrane is only a separator with no intrinsic catalytic activity (except for cases described by Liu and Au [9] and Paturzo et al. [19]), and the catalysts chosen for the reforming reaction usually have been noble metals (Ru, Rh, Pt), known to activate methane without inducing surface carbon deposition.

The effects of the use of a membrane reactor differ with the nature and properties of the membranes considered. With a mesoporous (8 nm) mullite membrane, having a low hydro-

---

[*] Corresponding author. Fax: +33 390 242 747.
E-mail address: ernstb@ecpm.u-strasbg.fr (B. Ernst).

0021-9517/$ – see front matter © 2007 Elsevier Inc. All rights reserved.
doi:10.1016/j.jcat.2007.09.022

gen selectivity with single gases (separation factor of 2 and 3 for H_2/CH_4 and H_2/CO_2, respectively), Ferreira-Aparicio et al. [13] observed no enhancement of methane and CO_2 conversion but found that the H_2/CO ratio was superior to that of a fixed-bed reactor. For membranes of Vycor glass and silica-coated Vycor glass, Prabhu et al. [14–16] found that more so than the membrane selectivity, the property of permeability plays a decisive role, although these authors underlined the fact that for membranes with the lowest permselectivity, a dilution effect must be taken into account. With a separation factor for mixed H_2/CH_4 gases lower than for Knudsen diffusion, Liu and Au [9] demonstrated a beneficial effect on methane conversion of the use of a catalytic membrane composed of La_2NiO_4 on zeolite. For metal (Pd and Pd–Ag)-based membranes, systematic enhancement of the conversion is observed with an increase of the H_2/CO ratio. However, Galuszka et al. [11] showed that palladium membranes are not suitable for this kind of high-temperature reaction, because the formation of carbon filaments and pinholes during the reaction destroys the metallic layer. Moreover, with palladium-based membranes, the strong interaction between hydrogen and palladium leads to the formation of a solid solution of hydrogen in palladium (α phase) and then, at higher hydrogen concentrations, to a hydride (β phase); the α-phase to hybrid β-phase transition at low temperature in the presence of hydrogen induces embrittlement of the Pd layer [20]. On the other hand, Munera et al. [10] have shown that this effect was absent for a Pd–Ag membrane with a Rh/Al_2O_3 catalyst.

The objective of this work was the development in a membrane reactor for the dry reforming of methane of a nickel composite membrane, stable at high temperatures while retaining high hydrogen permselectivity. It was anticipated that strong surface interactions between nickel and hydrogen in a thin film, where surface diffusion would be dominant, might enable selective permeation. Limited studies [21–23] of nickel membranes based on amorphous Ni–P and Ni–B as gas separators have shown them to be unstable at high temperatures due to a transition from amorphous to metallic phases. Thus, for the present work, we chose a thin pure nickel film deposited on a tubular and asymmetric alumina support by electroless plating.

In most instances, the membrane was associated with a catalyst, in a packed-bed configuration, required to activate the methane conversion. Kikuchi and Chen [12] showed that the catalytic activity of several metals in a membrane reactor decreased in the order Ni > Rh,Pt > Pd > Ru > Ir (*alumina support*). Thus, due to its high activity and low price, nickel seems to be the best choice, although there is evidence that it is susceptible to coke formation [12,18,24–27] resulting from methane decomposition ($CH_4 \leftrightarrow C + 2H_2$; $\Delta H^\circ_{\text{reaction}}(298\ \text{K}) = 74.8\ \text{kJ/mol}$), syngas reaction ($CO + H_2 \leftrightarrow C + H_2O$; $\Delta H^\circ_{\text{reaction}}(298\ \text{K}) = -131.3\ \text{kJ/mol}$) and the Boudouard reaction ($2CO \leftrightarrow C + CO_2$; $\Delta H^\circ_{\text{reaction}}(298\ \text{K}) = -172.1\ \text{kJ/mol}$). This last reaction, favored by transition metals including Fe and Ni, is the principal cause of graphitic carbon formation in packed-bed reactors [12,25,28,29] and results from an excess of carbon monoxide produced by the RWGS ($CO_2 + H_2 \leftrightarrow CO + H_2O$). Thus, in this work, we decided to add cobalt to supported nickel-based catalysts because of its higher resistance to coking [30]. An inherent advantage of a supported catalyst is the dispersion of active sites, because aggregation of Ni centers favors coking [31].

The purpose of the present work was to point out, using the thermodynamic data, the beneficial effects of a nickel membrane reactor compared with a packed-bed reactor for both Ni/Al_2O_3 and $Ni–Co/Al_2O_3$ catalysts in terms of methane and CO_2 conversions, syngas production levels, and catalyst coking resistance.

2. Experimental

2.1. Membrane materials

The support chosen was a Pall Exekia Membralox® type membrane (T1.70) of an asymmetric, tubular geometry, 25 cm long with an outer diameter of 10 mm and an inner diameter of 7 mm. It contained four concentric layers decreasing in thickness and porosity from the tube center. The layer with the smallest pore size was a mesoporous γ-alumina film, with an estimated thickness of 3–4 µm. The average pore size of this layer was estimated as 4.7 nm.

To obtain the nickel/ceramic membrane, the metal was deposited by electroless plating. The method, well adapted to the tubular support geometry, is based on the catalytic reduction of a metastable nickel complex on the alumina support surface using hydrazine as a reducing agent. After the support surface was cleaned, it was activated by deposition of Pd nuclei produced by Sn(II) reduction of $[Pd(NH_3)_4]^{2+}$ [32] and the whole support dried at 120 °C for 12 h before deposition of the final metal (Ni) layer by electroless plating. In this key final step, the outer part of the membrane was covered by Teflon and placed in the electroless bath (Table 1 gives compositions). $[Pd(NH_3)_4](NO_3)_2$ is a convenient reagent for Pd deposition [33], and hydrazine is particularly useful reducing agent for deposition on a porous substrate [33,34]. Disodium-dihydrogen ethylenediaminetetraacetate (Na_2H_2EDTA) is a widely used sequestrant [35] suitable for Ni(II). The deposition time was 3 h (at 75 °C) for the Ni-based plating bath. After the deposition, the membrane was rinsed with demineralized water, dried for 12 h at 120 °C, and weighed. Heat treatment under a reducing gas mixture (5% H_2/95% He) at 900 °C was used to stabilize the Ni/ceramic membrane. More details on the preparation and characterization of the Ni/ceramic composite membrane are available elsewhere [36].

Table 1
Composition and operating conditions of the electroless plating bath

Composition	Concentration	Experimental conditions
Nickel acetate	0.12 mol/L	
Na_2EDTA, $2H_2O$	0.016 mol/L	
Lactic acid	0.15 mol/L ($d = 1, 2$)	
Sodium hydroxide	7.5 g/L	
Hydrazine hydrate	0.4 mol/L	
pH		9.6
Temperature		75 °C

2.2. Catalyst preparation

The catalysts Ni/Al_2O_3 and $Ni–Co/Al_2O_3$ were prepared by co-precipitation of the metal oxalates. Hydrated Ni(II), Co(II), and Al(III) nitrates were combined in quantities corresponding to the final desired compositions of 33 wt% Ni/Al_2O_3 and 33 wt% $(Ni–Co)/Al_2O_3$, with a molar ratio Co:Ni of 1:1 for the latter. Each nitrate was separately dissolved in ethanol, and the solutions were heated to 70 °C before being mixed. Then, under vigorous stirring, oxalic acid dihydrate was added to cause precipitation of the mixed oxalates. The mixture of the precipitate composed of mixed Ni and/or Co and Al oxalates and the solvent was slowly evaporated to dryness. The prepared samples were then dried under mild vacuum at 60 °C for 4 h and finally calcined at 550 °C for 7 h.

2.3. Catalyst and membrane characterization

X-ray diffraction (XRD) measurements were performed using a Siemens Daco 500 powder diffractometer instrument with a CoK_α source ($\lambda = 0.1789$ nm). Patterns were recorded for 2θ 30–85° (2θ scale) with a 0.04° increments and 1 s exposure. Phases were identified using the Joint Committee on Powder Diffraction Standards (JCPDS) files.

Thermogravimetric analyses (TGA) were performed on a Setaram 92-12 thermogravimeter. The sample was placed in an alumina crucible under air flow (15 $\mathrm{mL\,min^{-1}}$) with a temperature ramp of 4 $\mathrm{K\,min^{-1}}$ from 20 to 900 °C. Specific surface area measurements of the catalysts were performed with a Coulter SA 3100 porosimeter. The BET specific area and the pore volume were deduced from the N_2 adsorption/desorption isotherms at 77 K. The microporous volume and the pore repartition were determined by the t-plot and BJH methods.

Temperature-programmed reduction (TPR) experiments were done by passing a gas mixture of 3.2% hydrogen in argon over the calcined catalyst at a total flow rate of 50 $\mathrm{mL\,min^{-1}}$ between 30 and 900 °C (heating rate: 15 $\mathrm{°C\,min^{-1}}$). A TCD device monitored the hydrogen consumption.

The surface morphology and the thickness of nickel layers were observed by scanning electron microscopy (SEM) (JEOL JSM-6700F, FEG). The SEM images were obtained with an extraction voltage of 3–15 kV and a working distance of 6–18 mm. Microstructural information was obtained using high-resolution transmission microscopy (HRTEM). The catalysts were examined under a TOPCON 002B microscope operating at 200 kV (resolution of 0.18 nm).

2.4. Hydrogen permselectivity

The flux and the selectivity of the membrane were evaluated for both single gases and gas mixtures. The alumina support membrane and nickel membrane were tested with pure hydrogen or nitrogen and with an equimolar mixture of both gases. The experimental setup is shown in Fig. 1. The same unit was used for the catalytic tests. The flow rates of the inlet homogeneously mixed gases (N_2, H_2/CH_4, CO_2) were regulated by Brooks 5850 TR mass flow controllers. A tubular stainless steel reactor in which a quartz tube (for fixed-bed catalytic tests) or a membrane (for permselectivity measurements and catalytic membrane reaction tests) could be placed, was heated using a Thermocoax high-temperature resistant heating wire and a West 820 temperature regulator. A co-current sweep gas (argon) was used in the external compartment. The transmembrane pressure difference was regulated using an Edwards ASG 2000 pressure gauge, a Keller numerical manometer (1–30 bar), and a Nupro pressure regulator. The permeate side was maintained at atmospheric pressure. The gas flow rates were measured by a digital bubble-flow meter. Composition of the outlet gases (permeate and retentate) was determined using a computer-controlled online Agilent Technologies M200 gas microchromatograph.

The permeability property, defined as the ability of a gas to permeate through the membrane, was calculated from the measured permeate flux. This flux J_i of a gas i can be given in $\mathrm{mol\,m^{-2}\,s^{-1}}$. The selectivity was evaluated by calculating the separation factor, $\alpha_{i/j}$, corresponding to the molar fraction of the species i and j to be separated in the permeate and in the feed:

$$\alpha_{i/j} = \frac{(\frac{x_i}{x_j})_{\text{permeate}}}{(\frac{x_i}{x_j})_{\text{feed}}}.$$

These separation factors were compared with those of Knudsen diffusion, for which the separation factor between gas i and j can be written as follows:

$$\alpha_{i/j} = \sqrt{M_j/M_i} \quad \text{with } M_j > M_i.$$

2.5. Catalytic tests

The catalytic tests were done in two reactor configurations: first in a packed-bed reactor (without membrane/with a quartz tube), and then in a nickel membrane reactor, to compare the results in each configuration. Fig. 2 shows the membrane reactor configuration. Before reaction, 200 mg of the catalysts were reduced in situ at 500 °C under 50% H_2/50% N_2 for 10 h for both types of reactors. The temperature was then decreased to 400 °C, and the reactants and the carrier gas were brought into contact with the catalyst to begin the experiment. The reactant flow rate was 50 $\mathrm{mL\,min^{-1}}$ with a ratio $CH_4/CO_2 = 1$ (10% CH_4; 10% CO_2; 80% N_2) under atmospheric pressure, whereas the catalyst was placed in a fixed-bed configuration with a contact time of 0.45 $\mathrm{s^{-1}}$ and a GHSV of 3000 $\mathrm{h^{-1}}$. The catalytic tests were carried out between 400 and 550 °C.

The conversion of the reactants was calculated with the following formulas [37]:

- Packed-bed reactor,

$$CH_4(\%) = \frac{F_{CH_4,\text{in}} - F_{CH_4,\text{out}}}{F_{CH_4,\text{in}}} \times 100, \tag{1}$$

$$CO_2(\%) = \frac{F_{CO_2,\text{in}} - F_{CO_2,\text{out}}}{F_{CO_2,\text{in}}} \times 100; \tag{2}$$

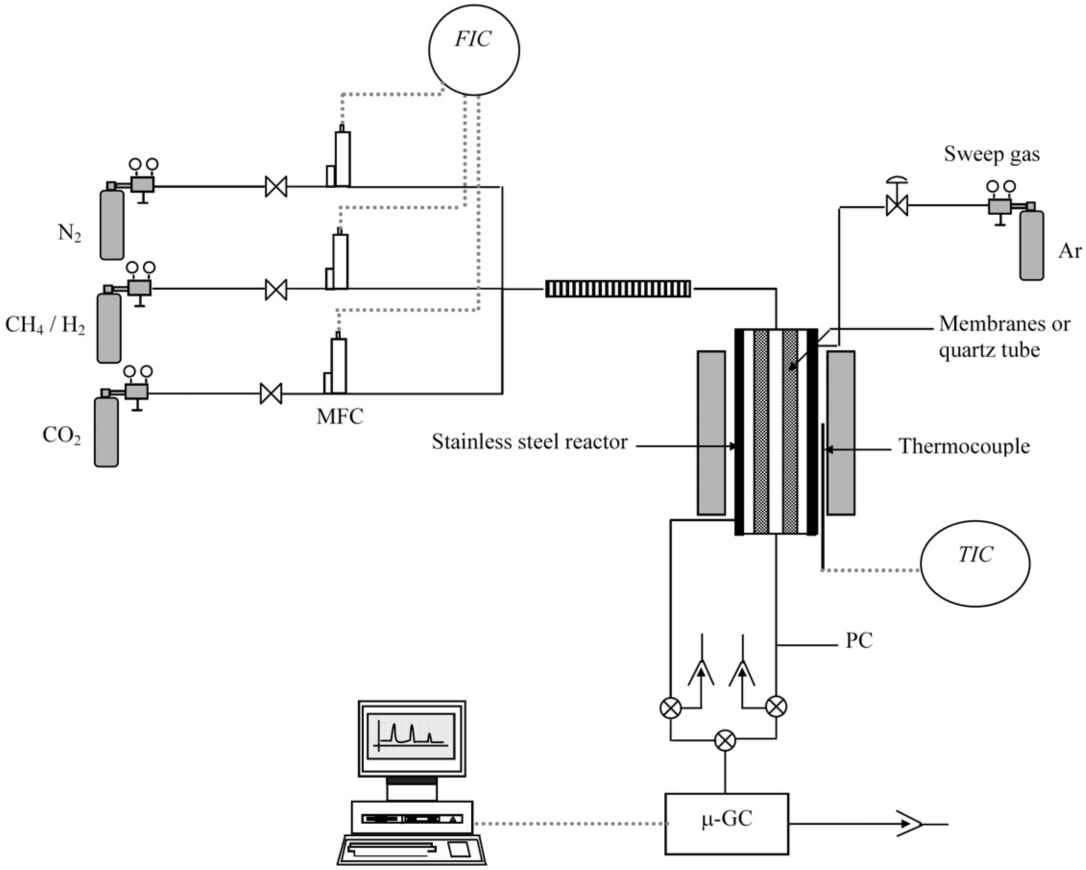

Fig. 1. Experimental device for the catalytic tests for the different reactor configurations.

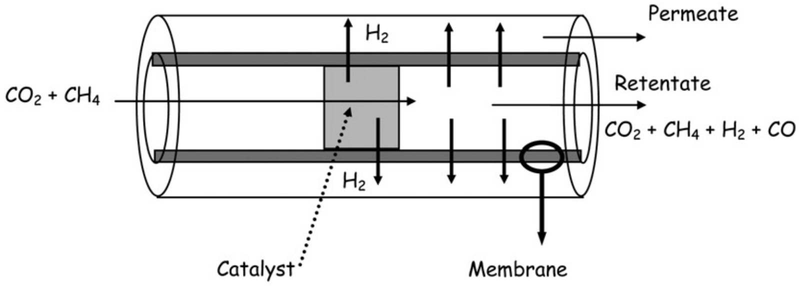

Fig. 2. Schematic representation of the membrane reactor configuration for the dry reforming of methane.

- Membrane reactor,

$$CH_4(\%) = \frac{F_{CH_4,\mathrm{in}} - F_{CH_4,\mathrm{permeate}} - F_{CH_4,\mathrm{retentate}}}{F_{CH_4,\mathrm{in}}} \times 100, \tag{3}$$

$$CO_2(\%) = \frac{F_{CO_2,\mathrm{in}} - F_{CO_2,\mathrm{permeate}} - F_{CO_2,\mathrm{retentate}}}{F_{CO_2,\mathrm{in}}} \times 100 \tag{4}$$

with F_i: molar flow rate of gas i ($\mathrm{mol\,s^{-1}}$).

2.6. Chemical equilibrium calculations

Here we consider the thermodynamics of the multiple interconnecting equilibria that influence the CH_4 and CO_2 conversions. From knowledge of standard free energies and heat capacities, it is possible to calculate the value of a reaction equilibrium constant at any temperature. Appropriate data for the present calculations were drawn from reference [38].

If we consider the reaction of the dry reforming of methane $CH_4 + CO_2 \leftrightarrow 2CO + 2H_2$ and the RWGS reaction $CO_2 + H_2 \leftrightarrow CO + H_2O$, then the variables of the problem are the equilibrium displacements, X_1 and X_2, of the two reactions. The molar fractions of the different gases can be calculated from the extent of reaction and the initial number of mol, n_0, of each reactant, it being possible to dilute the system with N_2. Thus, the system of equations to solve with X_1 and X_2 as unknown quantities is

$$f_1(X_1, X_2) = \frac{(\frac{n_{CO}}{n_T})^2 \cdot (\frac{n_{H_2}}{n_T})^2}{(\frac{n_{CH_4}}{n_T}) \cdot (\frac{n_{CO_2}}{n_T})} - K_1 = 0,$$

$$f_2(X_1, X_2) = \frac{(\frac{n_{CO}}{n_T}) \cdot (\frac{n_{H_2O}}{n_T})}{(\frac{n_{CO_2}}{n_T}) \cdot (\frac{n_{H_2}}{n_T})} - K_2 = 0$$

with

$$\begin{aligned}
&n_{CH_4} = n_{CH_4,0} - n_{CH_4,0}X_1,\\
&n_{CO_2} = n_{CO_2,0} - n_{CH_4,0}X_1 - n_{CO_2,0}X_2,\\
&n_{CO} = 2n_{CH_4,0}X_1 + n_{CO_2,0}X_2,\\
&n_{H_2} = 2n_{CH_4,0}X_1 - n_{CO_2,0}X_2,\\
&n_{H_2O} = n_{CO_2,0}X_2,\\
&n_{N_2} = n_{N_2,0},\\
&n_{CH_4} = n_{CH_4,0} + n_{CO_2,0} + n_{N_2,0} + 2n_{CH_4,0}X_1.
\end{aligned}$$

This system of two simultaneous nonlinear equations was solved by Newton's method, each function being linearized as a two-dimensional Taylor series (using MATLAB functions and programs [39]).

3. Results and discussion

3.1. Membrane characterization

The XRD pattern (Fig. 3a) of the alumina support shows only detectable peaks for the α-alumina phase (JCPDS: 71-1126; rhombohedral system [40]) and none for the γ-alumina, presumably because of the very small size of the grains composing its layer. For the electroless plating preparation of the Ni/ceramic composite membrane, hydrazine was used as reducing agent, as for Ni deposition on zirconia powder [41] and on metals [42]. The deposition of the metal on the activated support led to the penetration and covering of the γ-alumina film by the nickel. Heat treatment at 900 °C under a reducing flux (H_2/N_2) was applied to sinter the metal and increase the migration of the metal atoms present in the pores of the alumina to the external side of the support surface. The XRD pattern of the nickel/ceramic membrane showed peaks (Fig. 3b) for metallic Ni (JCPDS 4-0850) that became sharper and more intense after the heat treatment (Fig. 3c). Peaks with very low intensity were seen for α-alumina. SEM showed that the microstructure of the membrane was homogeneous after the heat treatment (Fig. 4). The estimated thickness of the nickel layer was 1–1.5 µm [43].

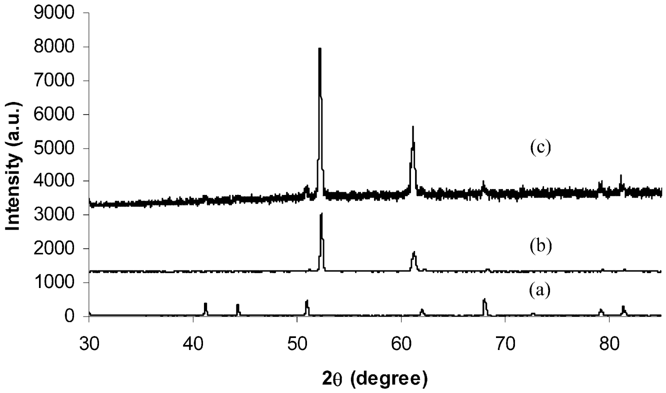

Fig. 3. X-ray diffraction patterns of (a) the alumina support, (b) the nickel composite membrane after electroless plating and (c) the nickel composite membrane after heat treatment at 900 °C.

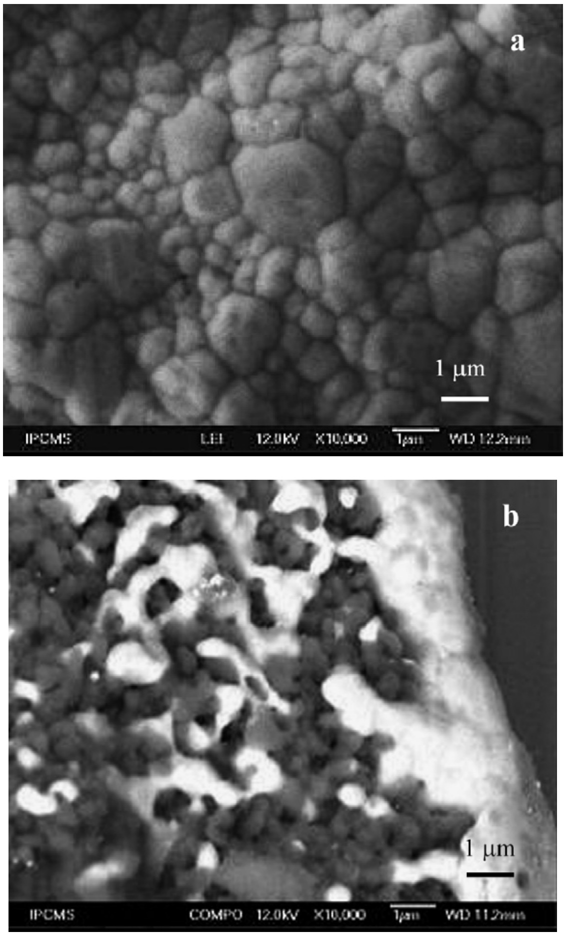

Fig. 4. SEM images of (a) the nickel composite membrane microstructure and (b) cross-sectional view.

3.2. Hydrogen permselectivity

Metals like palladium, platinum, and nickel are well known to have a strong surface interaction with hydrogen, and membranes made with palladium were the first shown to exhibit high hydrogen permselectivity at high temperatures. Platinum membranes also have been used in high-temperature hydrogen separation and show promising properties [1,44]; however, high cost is a big drawback with both Pd and Pt, making Ni an interesting alternative.

The hydrogen permselectivity of the γ-alumina mesoporous film was first tested for a single gas. The separation factors varied from 2 at room temperature to 2.5 at 500 °C, and the permeation principally involved two contributions: viscous flux and Knudsen diffusion. The small separation factors found are of the same order of magnitude as that reported in the literature for mesoporous membranes of similar thickness and pore size distribution [24,26]. For a gas mixture as feed, the γ-alumina mesoporous layer showed no separation at any of the temperatures investigated.

The nickel layer improves the hydrogen selectivity of the alumina support despite the thinness of the metallic layer. It has been demonstrated previously that surface diffusion is the main mechanism for transport of hydrogen through the nickel membrane [43] and that the H_2/N_2 separation factor is of 11.7 at 600 °C using a mixture of both gases as feed and argon as sweep gas. However, nitrogen and hydrogen also permeate through the membrane through Knudsen diffusion (Fig. 5).

3.3. Prediction of the thermodynamic equilibrium (CH_4 and CO_2 conversions, H_2 and CO productions)

To assess the performance of a membrane reactor, the equilibrium state that the system should attain is essential knowledge. Our analyses were based on treatment of the system as involving dry reforming of methane as the main reaction accompanied by the RWGS as a side process:

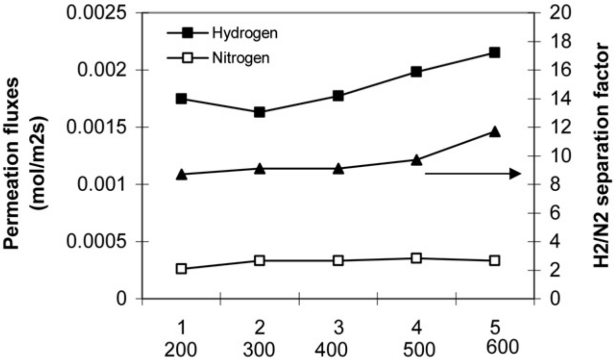

Fig. 5. Hydrogen and nitrogen permeation fluxes and H_2/N_2 separation factors for the nickel composite membrane.

$$CH_4 + CO_2 \leftrightarrow 2CO + 2H_2,\quad \Delta H^\circ_{\text{reaction}}(298\ \text{K}) = 247.3\ \text{kJ/mol}, \qquad \text{(reaction 1)}$$

$$CO_2 + H_2 \leftrightarrow CO + H_2O,\quad \Delta H^\circ_{\text{reaction}}(298\ \text{K}) = 41.0\ \text{kJ/mol}. \qquad \text{(reaction 2)}$$

Graphite formation reactions must be also considered because of their importance in catalyst poisoning but processes of particular relevance to the present system such as

$$CH_4 \leftrightarrow C + 2H_2,\quad \Delta H^\circ_{\text{reaction}}(298\ \text{K}) = 74.8\ \text{kJ/mol}, \qquad \text{(reaction 3)}$$

$$2CO \leftrightarrow C + CO_2,\quad \Delta H^\circ_{\text{reaction}}(298\ \text{K}) = -172.1\ \text{kJ/mol}, \qquad \text{(reaction 4)}$$

$$CO + H_2 \leftrightarrow C + H_2O,\quad \Delta H^\circ_{\text{reaction}}(298\ \text{K}) = -131.3\ \text{kJ/mol}, \qquad \text{(reaction 5)}$$

$$CO_2 + 2H_2 \leftrightarrow C + 2H_2O,\quad \Delta H^\circ_{\text{reaction}}(298\ \text{K}) = -90.1\ \text{kJ/mol}, \qquad \text{(reaction 6)}$$

need not be considered separately, because they are not all independent, reaction 5, for example, simply being the sum of reactions 2 and 4.

The equilibrium constants for the 6 reactions are given in Table 2 for temperatures of 400 to 800 °C. Except for methane decomposition (reaction 3), these reactions have high equilibrium constants compared with those of reactions 1 and 2 at temperatures below 600 °C. For example, if the main reaction 1 is coupled with reactions 4 or 5, then a large part of the carbon monoxide formed during the dry reforming of methane should

Table 2

Chemical equilibrium constants as a function of temperature for the dry reforming of methane, the reverse water gas shift and the carbon formation reactions

Temperature (°C)	Equilibrium constant		
	K_1	K_2	K_3
	$CH_4 + CO_2 \leftrightarrow 2CO + 2H_2$	$CO_2 + H_2 \leftrightarrow CO + H_2O$	$CH_4 \leftrightarrow C + 2H_2$
400	4.985×10^{-6}	8.369×10^{-2}	6.811×10^{-2}
450	1.215×10^{-4}	1.338×10^{-1}	1.973×10^{-1}
500	1.972×10^{-3}	2.003×10^{-1}	1.1563
550	2.292×10^{-2}	2.839×10^{-1}	2.4303
600	2.0189×10^{-1}	3.850×10^{-1}	4.7385
650	1.4075	5.032×10^{-1}	6.4552
700	8.0455	6.374×10^{-1}	8.6640
750	38.8077	7.863×10^{-1}	11.4687
800	160.662	9.489×10^{-1}	14.9568

Temperature (°C)	Equilibrium constant		
	K_4	K_5	K_6
	$2CO \leftrightarrow C + CO_2$	$CO + H_2 \leftrightarrow C + H_2O$	$CO_2 + 2H_2 \leftrightarrow C + 2H_2O$
400	1.48×10^4	1.19×10^3	103.7
450	1.77×10^3	226.5	31.68
500	279.4	53.38	11.19
550	55.37	14.97	4.459
600	13.25	4.853	1.963
650	3.717	1.776	0.940
700	1.192	0.720	0.483
750	0.428	0.319	0.264
800	0.170	0.152	0.153

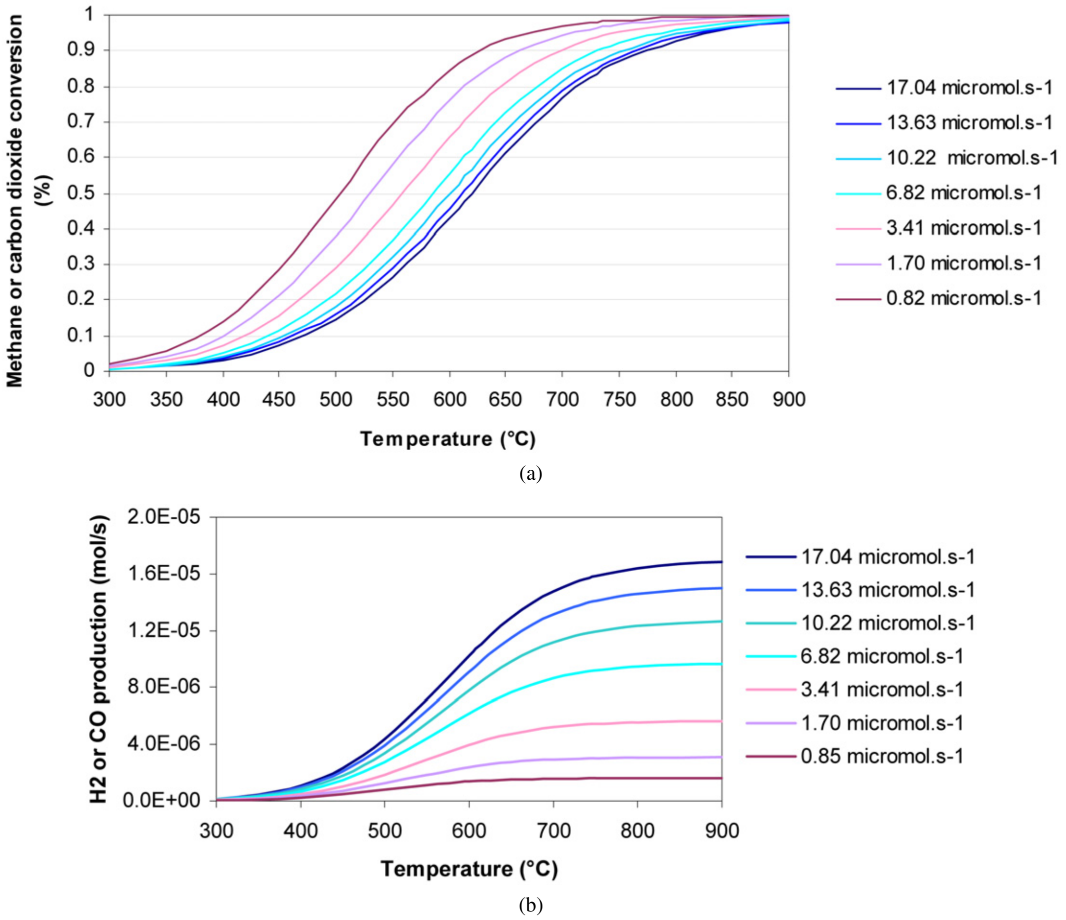

Fig. 6. Calculated temperature dependence of the methane or carbon dioxide equilibrium conversion (a) and of the hydrogen and carbon monoxide equilibrium levels (b) (dry reforming reaction only) for different methane feed flow rates (total feed flow rate: 34.082 μmol s^{-1}).

be consumed by the side reactions, leading to carbon formation. However, at temperatures above than 650 °C, the formation of graphitic carbon by decomposition of methane is favored thermodynamically compared with the other reactions (4, 5, and 6). Thus, on a thermodynamic basis, it must be concluded that dry reforming of methane is not favorable relative to graphite formation, underlining the potential importance of catalysts in selectively enhancing reaction rates.

In the following section, only the influence of the RWGS reaction on that of reforming is considered. The first parameter explored here was the dilution of the reactants for a constant total feed flow rate, because the increase in conversion obtained for porous membranes reactors could essentially come from the dilution of the feed. The beneficial effect of using a membrane rather than a packed-bed reactor was assessed generally in terms of combined increases of methane and carbon dioxide conversion and syngas production. The predicted effect of reactant feed dilution, as a function of the temperature on methane and carbon dioxide conversions is shown in Fig. 6a (reforming reaction only). Methane and carbon dioxide conversions are strongly influenced by the concentration of the reactant in the feed flow and increase dramatically with its increase, especially between 400 and 700 °C. For example, a fourfold dilution of the reaction mixture enhances methane conversion at 500 °C by a factor of 2, but both hydrogen and carbon monoxide production are obviously lower with increasing dilution (Fig. 6b).

If the reforming reaction is associated with the RWGS reaction, then the methane conversion is little affected by the contribution of the RWGS reaction whatever the dilution (Fig. 7a). Nevertheless, below 500 °C, methane conversion appears higher when is combined with the RWGS, whereas above 550 °C, this is not so. The difference in conversions is greater in more concentrated mixtures. In contrast, the carbon dioxide conversion rises when the main reaction is combined with the RWGS reaction (Fig. 7b), and this effect is more important at lower temperatures and in more concentrated mixtures. Hydrogen production (Fig. 8a) decreases because of the hydrogen consumption by the RWGS, whereas the CO_2 production (Fig. 8b) is clearly higher (Table 3). Although the experimental measurements showed that not all could be explained by the simultaneous occurrence of just the reforming and RWGS reactions, these simple predictions are close to reality and provide a useful basis for interpretation of the tests of the catalyst systems. In the literature, it has been established that several catalysts produce product distributions close to those equilibrium, and thus dry methane reforming is more limited by equilibrium than by kinetic factors. Consequently, use of the membrane reactor should allow working at isoconversion with lower temperatures but where carbon formation is more favored.

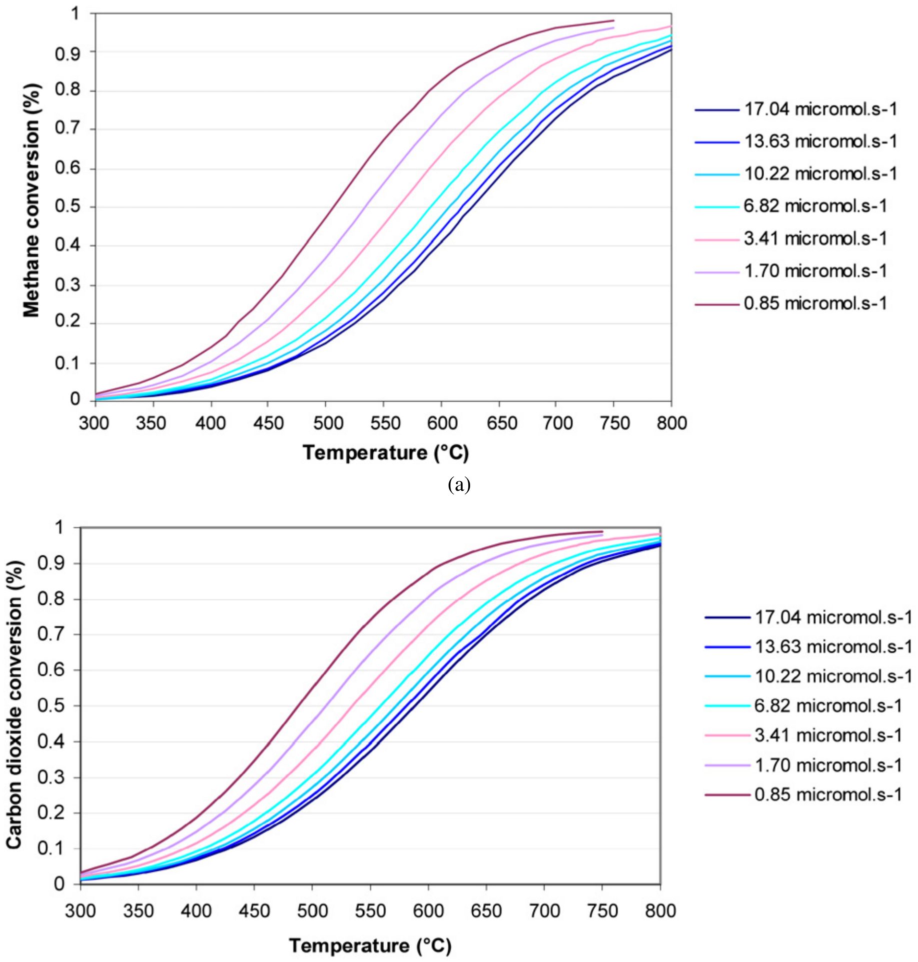

(a)

(b)

Fig. 7. Calculated temperature dependence of the methane (a) and carbon dioxide (b) equilibrium conversion in function of the temperature (dry reforming reaction + reverse water gas shift reaction) for different methane feed flow rates (total feed flow rate: 34.082 μmol s^{-1}).

Table 3

Theoretical equilibrium CH_4 and CO_2 conversions and H_2 and CO production levels for the dry reforming of methane coupled with or without the reverse water gas shift (reactant dilution: 80%)

T (°C)	Conversion (%)						Production (μmol s^{-1})					
	Reforming without RWGS			Reforming with RWGS			Reforming without RWGS			Reforming with RWGS		
	CH_4	CO_2	R_{CH_4/CO_2}	CH_4	CO_2	R_{CH_4/CO_2}	H_2	CO	$R_{H_2/CO}$	H_2	CO	$R_{H_2/CO}$
400	7.2	7.2	1	7.4	11.6	0.64	0.486	0.486	1	0.360	0.640	0.56
450	15.5	15.5	1	15.5	22.2	0.70	1.024	1.024	1	0.805	1.249	0.64
500	28.9	28.9	1	28.4	37.4	0.76	1.861	1.861	1	1.538	2.122	0.72
550	46.9	46.9	1	45.4	55.5	0.82	2.921	2.921	1	2.521	3.152	0.80

Note. CH_4/CO_2 ratio = 1; methane feed flow rate = 3.408 μmol s^{-1}, total feed flow rate = 34.082 μmol s^{-1}.

3.4. *Choice and characterization of the Ni/Al_2O_3 and $Ni–Co/Al_2O_3$ catalysts*

Reaction conditions for membrane reactors differ in general from those in a conventional packed-bed reactor (lower temperatures, hydrogen removal). The typical temperature range for dry reforming of methane in a packed-bed reactor is 750–800 °C [45–47]. However, the properties of the catalysts should be the same for both reactors. Hence, for both fixed-bed [48,49] and membrane [1] reactors, it has been shown that Ni/Al_2O_3 is one of the most active catalysts despite the ease of coke formation on its surface. Our aim was to prepare catalysts giving CH_4 and CO_2 conversions close to equilibrium under our experimental conditions (400 °C < T < 550 °C). To ensure that high conversions could be attained at lower temperatures, a high metal loading (33 wt%) was deposited on alumina support leading to the Ni/Al_2O_3 catalyst; cobalt was combined with nickel in a 1:1 molar ratio in the $Ni–Co/Al_2O_3$ catalyst.

The TGA/TDA curves before calcination of the dried $Ni–Co/Al_2O_3$ (Fig. 9a) and the Ni/Al_2O_3 (Fig. 9b) samples showed

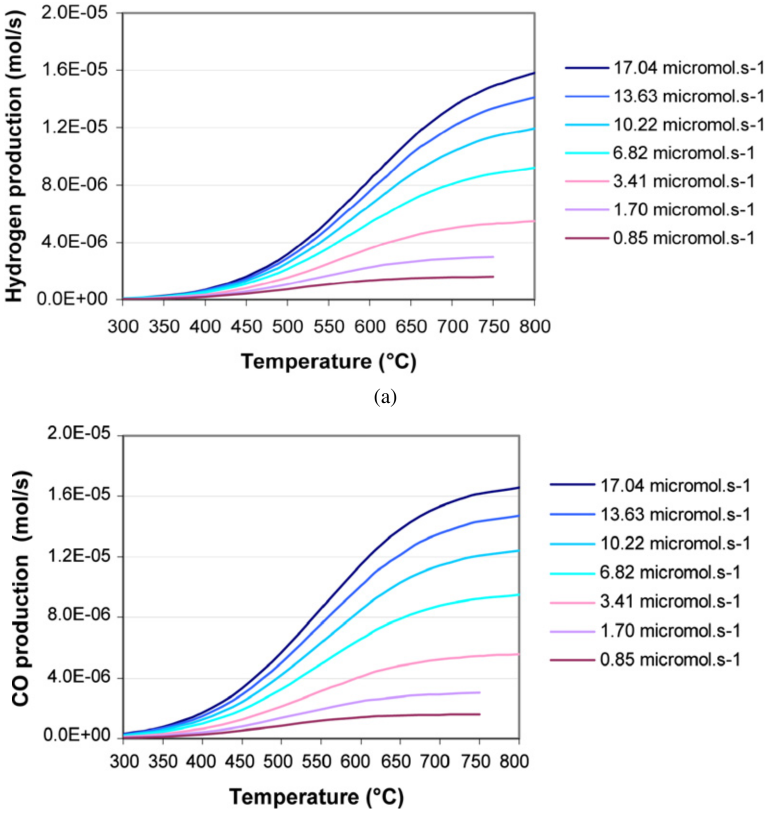

(a)

(b)

Fig. 8. Calculated temperature dependence of (a) hydrogen and (b) carbon monoxide equilibrium levels (dry reforming reaction + reverse water gas shift reaction) for different methane feed flow rates (total feed flow rate: 34.082 μmol s^{-1}).

a major endothermic peak corresponding to a loss of water between 100 and 200 °C. In addition, two endothermic peaks (220 and 380 °C) were observed due to the decomposition of oxalate. For both preparations, the weight losses occurred below 500 °C, and thus final calcinations in air were conducted at 550 °C.

After calcination, the specific surface areas were 215 $m^2\,g^{-1}$ for the Ni/Al_2O_3 catalyst and 138 $m^2\,g^{-1}$ for Ni–Co/Al_2O_3 catalyst. The estimated pore volumes were 0.18 $cm^3\,g^{-1}$ for the Ni/Al_2O_3 sample and 0.14 $cm^3\,g^{-1}$ for the Ni–Co/Al_2O_3 sample. Using the t-plot method, the results demonstrate that both catalysts were mesoporous with no microporous contribution. The pore size distributions were homogeneous, with 77 and 63% of pores with diameters <6 nm, respectively. Thus, due to the large specific surface of the catalysts, we presume that nickel and/or cobalt oxides were well dispersed on the alumina support.

The X-ray diffraction patterns of Ni/Al_2O_3 and Ni–Co/Al_2O_3 catalysts after calcination are given in Fig. 10. Crystalline NiO (JCPDS file 73-1519) was detected in the Ni/Al_2O_3 sample; its broad and weak peaks indicate that it was well dispersed. For the Ni–Co/Al_2O_3 catalysts, the NiO phase was not observed, but aluminate phases, $NiAl_2O_4$ (JCPDS file 71-963) and $CoAl_2O_4$ (JCPDS file 82-2251), were, indicating that a strong metal–support interaction was produced by the calcination.

The catalytically active species in methane reforming is the metal [50,51]. Thus, it was important to establish conditions for reduction of the metal ion centers in the calcined mixed oxides. To facilitate interpretation of the temperature-programmed reduction curves (Fig. 11), comparison was made with a Co/Al_2O_3 sample prepared in exactly the same way as the Ni/Al_2O_3 material. After calcination, an aluminate phase ($CoAl_2O_4$) was detected by XRD, and TPR curves showed that an important amount of hydrogen was consumed at about 900 °C for both cobalt-based preparations, corresponding to the reduction of the aluminates. The reduction of the Ni/Al_2O_3 catalyst occurred over a wider range of temperatures (400–800 °C). Although only the NiO phase was detected by XRD, it is possible that the structure of this catalyst is heterogeneous, with the presence of nickel aluminates that are probably well dispersed and thus too dilute to be detected by XRD. The degree of reduction for both catalysts is >90% at 900 °C. The XRD patterns after the reduction process (Fig. 12) showed mainly metal species; nevertheless, the aluminate phases remained for cobalt-based samples. It seems that the cobalt aluminates are less reducible than the nickel aluminates. A rough estimate of the metallic nickel particle diameter in the Ni/Al_2O_3 of 7.5 nm (after reduction at 900 °C) was possible using the Debye–Scherrer equation. A similar estimate was not possible for the Ni–Co/Al_2O_3 catalyst, due to the coincidence of the Ni and Co diffraction peaks. The dispersion of the metal particles produced by reduction is assumed to be a critical factor in avoiding coking of the catalyst. The catalysts were reduced *in situ* membrane with a higher concentration of hy-

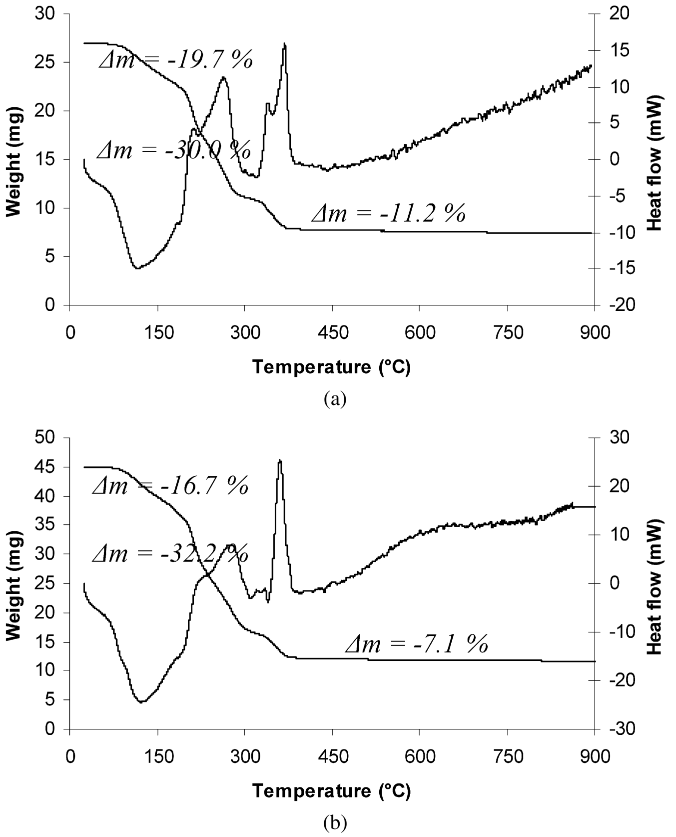

(a)

(b)

Fig. 9. TGA and TDA curves of the dried (a) Ni–Co/Al_2O_3 and (b) Ni/Al_2O_3 samples in synthetic air (heating rate: 4 K min^{-1}).

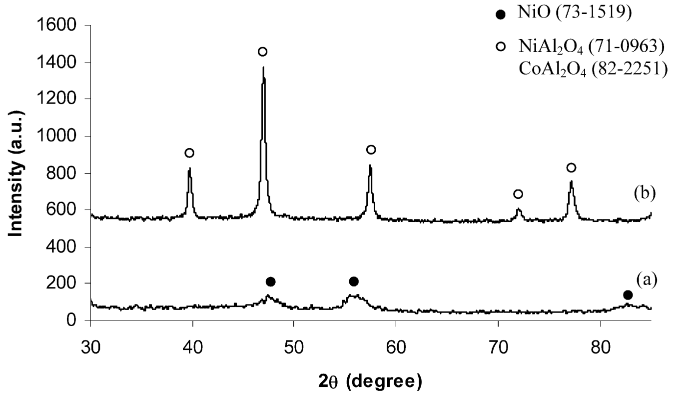

Fig. 10. XRD patterns for (a) the Ni/Al_2O_3 and (b) the Ni–Co/Al_2O_3 catalysts after calcination.

drogen and a lower heating rate than in the TPR conditions for both reactors at 500 °C, to preserve the state of the nickel composite membrane. The estimated reduction rates were 35% for the Ni/Al_2O_3 catalyst and 10% for the Ni–Co/Al_2O_3 catalysts.

3.5. Dry reforming of methane

To the question “catalysis with membranes or catalytic membranes?” asked by Ross and Xue [52], an answer is that the first possibility is best for metallic layers that are dense or contain only nanoscale defects. In fact, the low surface area of such membranes guarantees that they will not be effective catalysts, and, in the present systems, the Ni/ceramic composite membrane plays only the role of separator, because its specific surface area is too low to enable appreciable catalytic activity. To ensure its inertness, preliminary tests were done without catalyst; no catalytic activity was found under our operating conditions.

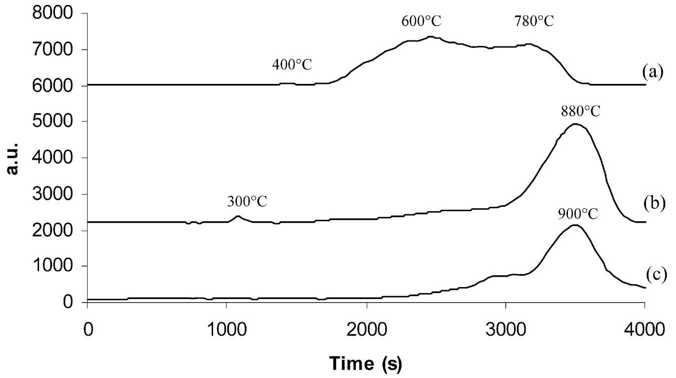

Fig. 11. TPR profiles for (a) the Ni/Al_2O_3 and (b) the Ni–Co/Al_2O_3 catalysts and (c) the Co/Al_2O_3 sample.

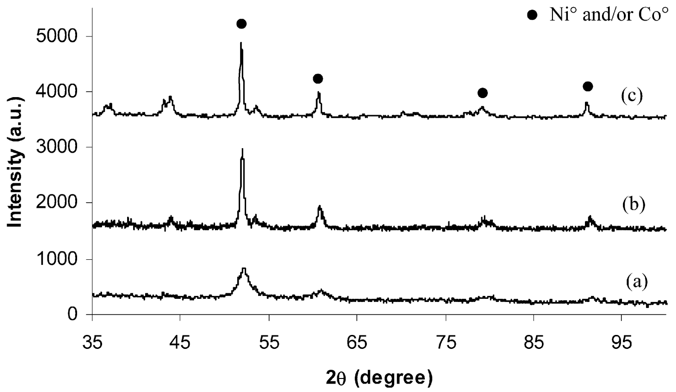

Fig. 12. XRD patterns for (a) the Ni/Al_2O_3 and (b) the Ni–Co/Al_2O_3 catalysts and (c) the Co/Al_2O_3 sample after temperature programmed reduction at 900 °C.

3.5.1. Packed-bed reactor

The catalytic results obtained for the Ni/Al_2O_3 packed-bed reactor are summarized in Table 4. This catalyst was particularly active at low temperatures. Whereas the R_{CH_4/CO_2} was near that predicted from equilibrium considerations (reforming reaction + RWGS reaction), the experimental $R_{H_2/CO}$ was clearly higher than the calculated value. These observations, coupled with the fact that all the ratios were greater than the equilibrium predictions, indicate that the RWGS reaction is not the only side reaction and that the Boudouard equilibrium (reaction 4), the reaction of decomposition of methane (reaction 3) and the reaction between CO/CO_2 and H_2 (reactions 5 and 6), producing mainly surface carbon, hydrogen, and water must have occurred. This assumption was verified by TEM. Indeed, the presence of carbon nanotubes (Fig. 13a1) was detected by XRD (Fig. 14a1) on the Ni/Al_2O_3 catalyst after reaction in the

Table 4
Experimental results for the Ni/Al_2O_3 catalysts tested in the packed-bed reactor, alumina membrane and nickel composite membrane reactor

Temperature (°C)	Conversion (%)								
	Alumina membrane reactor			Ni membrane reactor			Fixed bed		
	CH_4	CO_2	R_{CH_4/CO_2}	CH_4	CO_2	R_{CH_4/CO_2}	CH_4	CO_2	R_{CH_4/CO_2}
400	8.1	11.2	0.72	4.3	5.6	0.72	11.7	17.4	0.67
450	19.9	24.6	0.81	22.5	22.9	0.98	19.7	27.5	0.72
500	32.6	38.3	0.85	36.0	34.3	1.05	35.0	43.2	0.81
550	46.0	50.8	0.91	53.1	48.5	1.09	50.0	58.0	0.86

Temperature (°C)	Production (μmol s^{-1})								
	Alumina membrane reactor			Ni membrane reactor			Packed bed reactor		
	H_2	CO	$R_{H_2/CO}$	H_2	CO	$R_{H_2/CO}$	H_2	CO	$R_{H_2/CO}$
400	0.423	0.632	0.67	0.351	0.457	0.77	0.653	0.875	0.75
450	0.951	1.243	0.77	0.927	1.041	0.89	1.465	1.715	0.85
500	1.924	2.167	0.89	2.008	1.999	1.00	2.576	2.688	0.96
550	3.479	3.507	0.99	4.029	3.414	1.18	3.708	3.493	1.06

Note. Reaction conditions: pressure = 1 atm; CH_4/CO_2 ratio = 1; methane feed flow rate = 3.466 μmol s^{-1}; GHSV = 3000 h^{-1}.

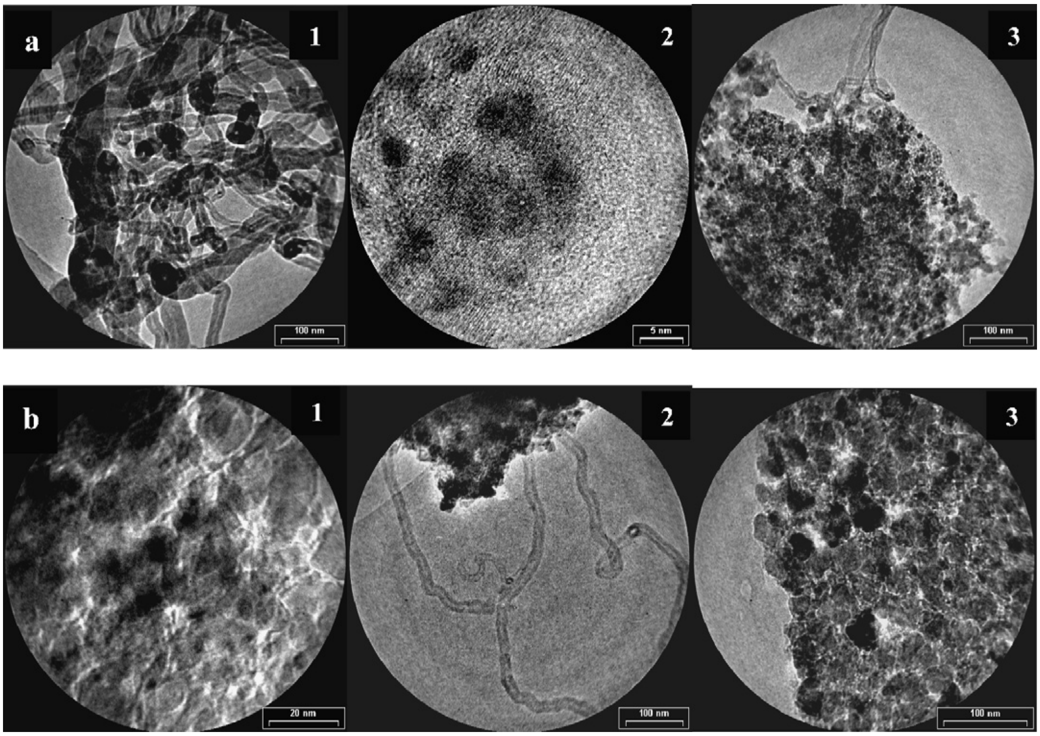

Fig. 13. TEM images of (a) the Ni/Al_2O_3 and (b) the $Ni–Co/Al_2O_3$ catalysts after catalytic tests in the packed-bed reactor (micrographs 1 and 2) and after catalytic tests in the membrane reactor (micrographs 3).

packed-bed reactor. The average Ni particle size was estimated as 5 nm by TEM (Fig. 13a2). This value is close to the estimated width of the nanotubes (6 nm), which have a thickness of about 15 nm. Literature evidence [53,54] indicates that these carbon structures with graphite basal planes parallel to the axis of the tube and with hemispherical caps at their ends are the result of the accumulation of large amounts of carbon on the catalyst which cause the break up of the nickel particles. According to the literature [55], a high coking rate is not always associated with the deactivation of catalysts of the present type, it being known that some sites can remain free for reactant activation, and the present systems perhaps need to be assessed for longer periods under reactant flow to detect instability of the conversions.

The results obtained for $Ni–Co/Al_2O_3$ catalyst packed-bed reactor are summarized in Table 5. Methane conversion was about 40% at 550 °C, whereas the R_{CH_4/CO_2} ratio was always less than unity. Aside from methane reforming, the secondary RWGS reaction is far from being negligible. In fact, it leads to a high carbon dioxide conversion with poor hydrogen selectivity ($S_{H_2} = 0.48$) at 550 °C. However, no deactivation of the catalyst was found during the reaction, and the carbon balance remained very close to 1 when the temperature increased. The X-ray diffraction pattern (Fig. 14b1) and the TEM images (Fig. 13b1) of

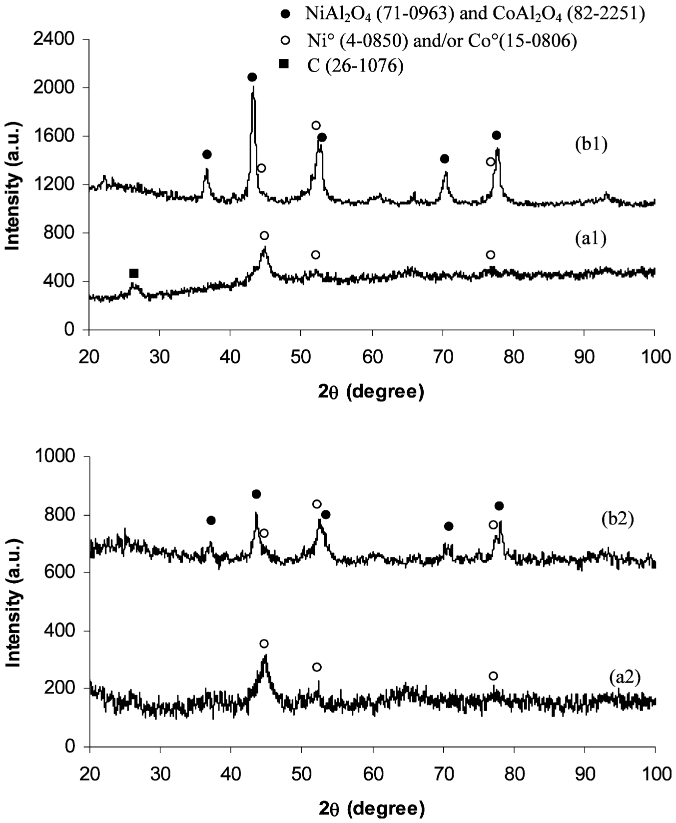

Fig. 14. XRD patterns for (a1) the Ni/Al_2O_3 and (b1) the $Ni–Co/Al_2O_3$ catalysts after catalytic tests in the packed-bed reactor and for (a2) the Ni/Al_2O_3 and (b2) the $Ni–Co/Al_2O_3$ catalysts after catalytic tests in the nickel composite membrane reactor.

the catalyst after reaction show that $<10\%$ of the metal (probably well anchored in the aluminate phases) was involved in the catalysis and that very little graphitic carbon was present (Fig. 13b2). The anchorage of the Ni° particles was probably the main reason of the coke formation resistance. Thus, the alumina support used in the present work was not only a dispersing agent, but also interacted strongly with metals by aluminate formation, thus restricting their surface mobility and inhibiting sintering.

3.5.2. *Alumina membrane reactor*

The catalyst reduction and the catalytic tests were conducted under the same conditions as for the packed bed. No sweeping gas was used in the outer compartment of the membrane reactor because of the high permeate rate. The results for the Ni/Al_2O_3 catalysts (Table 4) show, as in the packed bed, high activity, even with lower CH_4 and CO_2 conversions. This can be attributed to the low permselectivity of the alumina membrane allowing the diffusion of one part of the reactants through the membrane; this has been reported by Ferreira-Aparicio et al. [13] as well. The R_{CH_4/CO_2} and $R_{H_2/CO}$ ratios were higher for the alumina membrane reactor than for the packed-bed reactor, leading to the conclusion that the contribution of the side reactions was more limited.

The production of hydrogen and carbon monoxide was lower for the $Ni–Co/Al_2O_3$ catalyst than for the packed-bed reactor with the Ni/Al_2O_3 catalyst (Table 5). At 500 and 550 °C, methane conversion was equivalent in the two types of reactors, whereas CO_2 conversion was lower for the alumina membrane reactor. The close fit of the experimental and calculated (with the RWGS reaction) R_{CH_4/CO_2} and $R_{H_2/CO}$ ratios indicates that the side reactions of carbon formation were very limited.

The catalytic results can be compared to the literature reports using porous membrane reactors for the dry reforming of methane (Table 6). Consistent with our results, Ferreira-Aparicio et al. [13] have demonstrated that a membrane with low hydrogen selectivity is not able to significantly enhance the methane conversion. For zeolite [9] and Vycor glass [16] membranes, which have higher hydrogen selectivity, these authors attributed the increase in methane and carbon dioxide conversions not only to the removal of the hydrogen, shifting the equilibrium to H_2 and CO production, but also to the effect of dilution of the feed induced by using a sweep gas.

Table 5
Experimental results for the $Ni–Co/Al_2O_3$ catalysts tested in the packed-bed reactor, alumina membrane and nickel composite membrane reactors

Temperature (°C)	Conversion (%)								
	Alumina membrane reactor			Ni membrane reactor			Fixed bed		
	CH_4	CO_2	R_{CH_4/CO_2}	CH_4	CO_2	R_{CH_4/CO_2}	CH_4	CO_2	R_{CH_4/CO_2}
400	9.7	14.1	0.63	6.6	8.0	0.83	3.1	7.4	0.42
450	15.6	20.0	0.78	17.4	18.7	0.93	10.4	17.7	0.59
500	24.4	31.3	0.78	28.4	30.3	0.94	23.2	33.7	0.69
550	38.4	46.8	0.82	46.5	47.7	0.97	39.3	52.7	0.75

Temperature (°C)	Production ($\mu mol\,s^{-1}$)								
	Alumina membrane reactor			Ni membrane reactor			Fixed bed		
	H_2	CO	$R_{H_2/CO}$	H_2	CO	$R_{H_2/CO}$	H_2	CO	$R_{H_2/CO}$
400	0.139	0.243	0.57	0.487	0.669	0.73	0.215	0.368	0.58
450	0.479	0.785	0.61	1.147	1.308	0.88	0.660	0.917	0.72
500	1.382	1.764	0.78	2.263	2.356	0.96	1.535	1.806	0.85
550	2.806	3.194	0.88	3.655	3.655	1.00	2.778	2.986	0.93

Note. Reaction conditions: pressure = 1 atm; CH_4/CO_2 ratio = 1; methane feed flow rate = 3.466 $\mu mol\,s^{-1}$; GHSV = 3000 h^{-1}.

Table 6
Comparison of the catalytic results obtained with the γ-alumina membrane and the porous membranes described in the literature

Membrane	Separation factor		Catalyst	Reaction temp. (°C)	Conversion (%)		Reference
	H_2/CH_4	H_2/CO_2			CH_4	CO_2	
γ-Alumina	1.8	2.9	Ni–Co/Al_2O_3	550	38.4 (39.3)	46.8 (52.7)	This work
			Ni/Al_2O_3		46.0 (50.0)	50.8 (85.0)	
Mullite	2	3	Pt/Al_2O_3	550	16 (13)	25 (26)	Ferreira-Aparicio et al. [13]
Zeolite	7.8	5.6	Catalytic membrane	400	8.3 (8.5)	2.5 (2.7)	Liu and Au [9]
	5.4	4.6		600	47.9 (33)	40.6 (37)	
Vycor glass	2.76	4.26	Ni/MgO	650	70 (62.5)	– (73)	Prabhu et al. [16]
			Ni/La_2O_3		73 (62.5)	– (73)	

Note. ( ): packed-bed reactor conversion.

Table 7
Comparison of the catalytic results obtained with the nickel composite membrane and the palladium-based membranes described in the literature

Membrane	Layer thickness (μm)	Catalyst	W/F (g min mL^{-1})	Reaction temperature (°C)	Conversion (%)		Reference
					CH_4	CO_2	
Ni/ceramic	1.5	Ni–Co/Al_2O_3	3.33×10^{-4}	550	46.5 (39.3)*	47.7 (52.7)	This work
		Ni/Al_2O_3			53.1 (50.0)	48.5 (58.0)	
Pd	20	Ru/Al_2O_3	/	500	49.5 (/)	43.1 (/)	Kikuchi and Chen [12]
		Rh/Al_2O_3			62.2 (/)	45.3 (/)	
		Pd/Al_2O_3			55.3 (/)	52.0 (/)	
		Pt/Al_2O_3			61.3 (/)	52.5 (/)	
Pd	10	Pd/Al_2O_3	1.75×10^{-4}	550	37.5 (17.2)	51.0 (24.6)	Galuszka et al. [11]
Pd	50	Pt/Al_2O_3	/	550	40 (28)	/	Raybold and Huff [8]
Pd/Ag	/	0.6% Rh/La_2O_3	5×10^{-4}	550	33.9 (26.0)	41.0 (41.9)	Munera et al. [10]
		0.93% Pt/La_2O_3			31.3 (26.3)	41.3 (38.2)	
Pd/stainless steel	12–35	Ni/Al_2O_3	/	550	22.5 (17.2)	41.4	Ferreira-Aparicio et al. [55]
Pd/Ag	/	0.6% Rh/La_2O_3	1.02×10^{-5}	550	33.9	42.8	Irusta et al. [56]
		0.6% Rh/La_2O_3–SiO_2			33.7	44.5	

Note. ( ): packed-bed reactor conversion.

3.5.3. Nickel composite membrane reactor

The Ni/ceramic composite membrane was hydrogen-permselective at high temperature, but the first experiment done without a sweep gas in the external compartment showed no change compared to what was obtained in a conventional reactor. A very small amount of gas can go through the membrane, and even if the permeate is rich in hydrogen, the low permeability leads to no "membrane effect" on the methane conversion values. To improve the permeability of the membrane, a co-current argon sweep gas flow rate of 100 mL min^{-1} was used in the external compartment.

Although high for the packed-bed reactor, the methane conversion for the Ni/Al_2O_3 catalyst was higher still for the nickel composite membrane reactor at temperatures above 450 °C (Table 4). Moreover, the CO_2 conversion decreased, leading to a higher R_{CH_4/CO_2}; it seems that the RWGS contributed less than in the alumina membrane reactor. The $R_{H_2/CO}$ ratio >1 at temperatures of 500 and 550 °C may be due to nonconsumption of hydrogen by the RWGS reaction and/or to the methane decomposition reaction, which could be favored by the hydrogen removal using the permselective nickel membrane. The diffraction peak corresponding to the carbon (JCPDS file 26-1076) was not detectable in the XRD pattern (Fig. 14a2). This result was confirmed by the TEM observation (Fig. 13a3) showing the presence of less carbon nanotubes.

For the Ni–Co/Al_2O_3 catalyst, the results obtained with the nickel membrane reactor in this configuration show enhanced methane conversion at each reaction temperatures compared with what can be found with the conventional reactor (23% at 500 °C and 19% at 550 °C), as well as a significant increases in hydrogen and carbon monoxide production of 56 and 45% at 400 °C, 42 and 30% at 450 °C, 32 and 23% at 500 °C and 24 and 18% at 550 °C (Table 5). At 500 and 550 °C, the ratios R_{CH_4/CO_2} and $R_{H_2/CO}$ are close to 1, and the methane conversion in the membrane reactor corresponds to the calculated values for the dry reforming of methane only. Thus, we conclude that the secondary RWGS reaction is eliminated by the preferential removal of the hydrogen during the reaction. The absence of graphitic carbon was confirmed by XRD (Fig. 14b2) and TEM (Fig. 13b3), showing that the catalyst Ni–Co/Al_2O_3 does indeed have a high resistance to coking. As has been concluded for a Ni/$Ce_{0.5}Zr_{0.5}O_2$ catalyst [54], this particular property is due more to the catalyst's intrinsic ability to keep its surface free of inactive carbon than to the experimental conditions and the configurations of the reactor.

Comparison (Table 7) of the present and published results for dry reforming in palladium membrane reactors shows that the methane and carbon dioxide conversions are quite similar for Pd layers with a thickness 7–30 times greater than our nickel layer and with an equivalent W/F value. However, the

Table 8
Composition of the retentate and permeate during the reaction in the Ni/ceramic membrane reactor configuration

T (°C)	Composition of the retentate (μmol m^{-2} s^{-1})				Composition of the permeate (μmol m^{-2} s^{-1})				Separation factor (*estimated*)		
	CH_4	CO_2	H_2	CO	CH_4	CO_2	H_2	CO	H_2/CH_4	H_2/CO	H_2/CO_2
Ni–Co/Al_2O_3 catalyst											
400	667	675	63.7	140	69.5	50.6	47.2	12.3	7.1	8.4	9.9
450	588	599	152	273	63.2	42.6	109	24.6	6.7	7.9	10.1
500	509	515	285	495	56.9	34.8	230	41.1	7.2	9.7	11.9
550	376	384	470	760	45.8	28.4	361	71.9	6.3	8.1	10.4
Ni/Al_2O_3 catalyst											
400	665	716	40	92	109	77	40	12	6.1	7.8	9.2
450	513	540	97	204	98	68	114	33	6.1	7.2	9.3
500	412	455	194	372	93	63	263	83	6	6.1	9.7
550	302	362	329	623	68	44	588	154	7.9	7.2	14.6

enhancement of methane is particularly spectacular for palladium membrane reactors with high hydrogen selectivity [8,11]. In these cases, hydrogen extraction from the reaction side likely favors methane cracking. Indeed, Galuszka et al. [11] concluded that a Pd membrane reactor was not suitable for high-temperature methane dry reforming because of the alteration of the palladium layer due to carbon filaments formed on its surface. Similarly, Paturzo et al. [19] observed increasing carbon deposition with conversion for a double-layer Ru ceramic membrane. Their work also revealed the dilemma of the catalytic membrane, which must be hydrogen-selective and also have a high metallic surface area (dispersion) for high activity; it also underscored the problem of the thermal stability of the membrane and its resistance to coking. For the Ni composite membrane, the estimated separation factors for H_2/CH_4, H_2/CO and H_2/CO_2 during the harsh conditions of the reactions, about 7, 8 and 10, were higher than those obtained for a Knudsen diffusion process (Table 8). Due to its high thermal stability and mechanical strength, the nickel membrane was used for several catalytic tests without deterioration of the properties of the separating nickel layer being evident. Moreover, no argon (sweep gas) was detected in the internal compartment (retentate side), demonstrating that the beneficial effect observed with the nickel membrane reactor is due not to a dilution phenomenon, but rather to a real shift of the equilibrium caused by preferential removal of hydrogen during reaction in the nickel membrane reactor. After the catalytic test, no graphitic carbon was detected on the nickel layer by XRD (Fig. 15).

4. Conclusion

The main beneficial effect of using the nickel membrane reactor, resulting from the selective removal of hydrogen, is the elimination or limitation of the side RWGS reaction. This has different consequences depending on the catalytic materials. For the Ni/Al_2O_3 catalyst containing free metallic nickel with a particle size of about 5 nm, particularly sensitive to coking, with carbon nanotubes formed in the packed-bed reactor, the use of the membrane reactor led to an significant reduction in carbon deposition, due mainly to the limitation of the RWGS and consequently the inhibition of the Boudouard reaction, but not total elimination, probably because methane decomposition also is favored by hydrogen removal. For the Ni–Co/Al_2O_3 catalyst, where the metallic nickel is stabilized by the aluminate phase, restricting their surface mobility and inhibiting sintering, the resistance to coking is observed in both reactors. For this catalyst, elimination of the secondary RWGS reaction by the preferential removal of the hydrogen in the nickel membrane reactor allows a significant increase in methane conversion (+67% at 450 °C, +22% at 500 °C and +18% at 550 °C), combined with increased hydrogen production (+42% at 450 °C, +32% at 500 °C and +22% at 550 °C) compared with the results obtained in a packed-bed reactor.

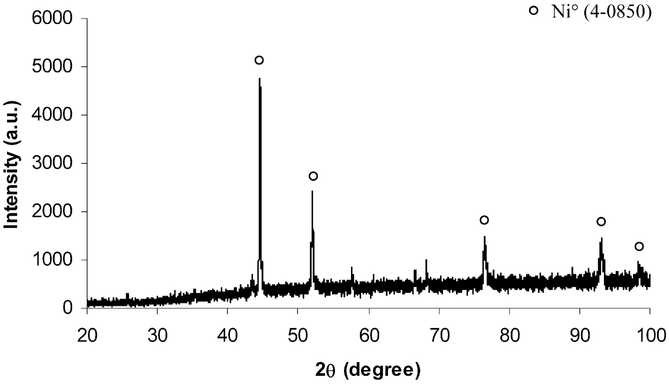

Fig. 15. XRD pattern of the nickel composite membrane after catalytic tests.

This first study on a nickel composite membrane applied to the dry reforming of methane also has demonstrated the high thermal stability of the microstructure of this membrane. With no intrinsic catalytic activity, the membrane kept its hydrogen selectivity during the catalytic tests with separation factors H_2/CH_4, H_2/CO and H_2/CO_2 higher than the values for Knudsen diffusion and estimated at 7, 8 and 10, respectively. Crucially, in regard to its potential for use in a high-temperature membrane reactor, the Ni surface underwent no significant alteration under catalytic reaction conditions, and thus offers an efficient alternative to the use of palladium-based membranes.

Acknowledgments

The authors thank Jack Harrowfield, ISIS/ULP for his help with elaboration of the manuscript, and to Y. Zimmermann, LMSPC/ECPM for the high-quality TEM images.

References

[1] E. Kikuchi, Y. Nemoto, M. Kajiwara, S. Uemiya, T. Kojima, Catal. Today 56 (2000) 75.
[2] J. Shu, B.P.A. Grandjean, S. Kaliaguine, Appl. Catal. A 119 (1994) 305.
[3] M. Chai, M. Machida, K. Eguchi, H. Arai, Appl. Catal. A 110 (1994) 239.
[4] S. Uemiya, N. Sato, H. Ando, T. Matsuda, E. Kikuchi, Appl. Catal. A 67 (1991) 223.
[5] S. Laegsgaard Jorgensen, P.E. Hojlund Nielsen, P. Lehrmann, Catal. Today 25 (1995) 303.
[6] J.S. Oklany, K. Hou, R. Hughes, Appl. Catal. A 170 (1998) 13.
[7] G. Marigliano, G. Barbieri, E. Drioli, Chem. Eng. Process. 42 (2003) 231.
[8] T.M. Raybold, M.C. Huff, AIChE J. 48 (2002) 1051.
[9] B.S. Liu, C.T. Au, Catal. Lett. 77 (2001) 67.
[10] J. Munera, S. Irusta, L. Cornaglia, E. Lombardo, Appl. Catal. A Gen. 245 (2003) 383.
[11] J. Galuszka, R.N. Pandey, S. Ahmed, Catal. Today 46 (1998) 83.
[12] E. Kikuchi, Y. Chen, Stud. Surf. Sci. Catal. 107 (1997) 547.
[13] P. Ferreira-Aparicio, I. Rodriguez-Ramos, A. Guerrero-Ruiz, Appl. Catal. A Gen. 237 (2002) 239.
[14] A.K. Prabhu, S.T. Oyama, J. Membr. Sci. 176 (2000) 233.
[15] A.K. Prabhu, A. Liu, L.G. Lovell, S.T. Oyama, J. Membr. Sci. 177 (2000) 83.
[16] A.K. Prabhu, R. Radhakrishnan, S.T. Oyama, Appl. Catal. A Gen. 183 (1999) 241.
[17] B.A. Tindall, U. Grimsehl, South Afr. J. Chem. Eng. 10 (1998) 22.
[18] A.A. Ponelis, P. van Zyl, Stud. Surf. Sci. Catal. 107 (1997) 555.
[19] L. Paturzo, F. Gallucci, A. Basile, G. Vitulli, P. Pertici, Catal. Today 82 (2003) 57.
[20] I.B. Elkina, J.H. Meldon, Desalination 147 (2002) 445.
[21] B. Liu, H. Li, Y. Cao, J.F. Deng, C. Sheng, S. Zhou, J. Membr. Sci. 135 (1997) 33.
[22] X. Changrong, G. Xiaoxia, L. Fanqing, P. Dindkun, M. Guangyao, Colloids Surf. A Physicochem. Eng. Aspects 179 (2001) 229.
[23] D. Xue, H. Chen, G.H. Wu, J.F. Deng, Appl. Catal. A Gen. 214 (2001) 87.
[24] J.R. Rostrup-Nielsen, J. Catal. 31 (1973) 173.
[25] J.B. Claridge, M.L.H. Green, S.C. Tsang, A.P.E. York, A.T. Ashcroft, P.D. Battle, Catal. Lett. 22 (1993) 299.
[26] S.C. Tsang, J.B. Claridge, M.L.H. Green, Catal. Today 23 (1995) 3.
[27] A.T. Ashcroft, A.K. Cheetmann, M.L.H. Green, P.D.F. Vernon, Lett. Nat. 352 (1991) 225.
[28] M. Audier, A. Oberlin, M. Oberlin, M. Coulon, L. Bonnetain, Carbon 19 (1981) 217.
[29] B.A. Raich, H.C. Foley, Appl. Catal. A Gen. 129 (1995) 167.
[30] P.E. Nolan, D.L. Lynch, A.H. Cutler, Carbon 32 (1994) 477.
[31] A. Bhattacharyya, J.B. Hall, C. Choi-Feng, in: Symposium on Coke Formation and Mitigation, 210th National Meeting, American Chemical Society, IL, August 1995.
[32] N. Feldstein, J.A. Weiner, Plating (1972) 140.
[33] J.N. Keuler, L. Lorenzen, R.N. Sanderson, V. Linkov, Plating Surf. Finish. 84 (1997) 34.
[34] D.K. Simpson, Metal Finishing 83 (4) (1985) 57.
[35] J. Shu, B.P.A. Grandjean, E. Ghali, S. Kaliaguine, J. Membr. Sci. 77 (1993) 181.
[36] S. Haag, M. Burgard, B. Ernst, Surf. Coat. Technol. 201 (2006) 2166.
[37] A. Basile, L. Paturzo, Catal. Today 67 (2001) 55.
[38] S.I. Sandler, Chemical and Engineering Thermodynamics, second ed., John Wiley & Sons, New York, 1989.
[39] A. Constantinides, N. Mostoufi, Numerical Methods for Chemical Engineers with MATLAB Applications, in: N.R. Amundson (Ed.), Prentice Hall International Series in the Physical and Chemical Engineering Sciences, University of Houston, Upper Saddle River, 1999, p. 45.
[40] L.W. Finger, R.M. Hazen, J. Appl. Phys. 49 (1978) 5823.
[41] G. Wen, Z.X. Guo, C.K.L. Davies, Scripta Mater. 43 (2000) 307.
[42] P. Steinmetz, S. Alperine, A. Friant-Constantini, P. Josso, Surf. Coat. Technol. 43/44 (1990) 500.
[43] B. Ernst, S. Haag, M. Burgard, J. Membr. Sci. 288 (2007) 208.
[44] M. Kajiwara, S. Uemiya, T. Kojima, E. Kikuchi, Catal. Today 56 (2000) 65.
[45] A.I. Tsyganok, T. Tsunoda, S. Hamakawa, K. Suzuki, K. Takehira, T. Hayakawa, J. Catal. 213 (2003) 191.
[46] B.Q. Xu, J.M. Wei, H.Y. Wang, K.Q. Sun, Q.M. Zhu, Catal. Today 68 (2001) 217.
[47] C. Courson, L. Udron, D. Swierczynski, C. Petit, A. Kiennemann, Catal. Today 76 (2002) 75.
[48] J.R. Rostrup-Nielsen, J. Catal. 31 (1973) 173.
[49] J.R. Rostrup-Nielsen, J.-H. Bak Hansen, J. Catal. 144 (1993) 38.
[50] T. Hayakawa, A.C. Anderson, M. Schimizu, K. Suzuki, K. Takehira, Catal. Lett. 22 (1993) 307.
[51] V.R. Choudhary, V.H. Rane, A.M. Rajput, Catal. Lett. 22 (1993) 289.
[52] J.R.H. Ross, E. Xue, Catal. Today 25 (1995) 291.
[53] P.E. Nolan, M.J. Schabel, D.C. Lynch, A.H. Cutler, Carbon 33 (1995) 79.
[54] J.B. Claridge, M.L.H. Green, S.C. Tsang, A.P.E. York, A.T. Ashcroft, P.D. Battle, Catal. Lett. 22 (1993) 299.
[55] P. Ferreira-Aparicio, M. Benito, K. Kouachi, S. Menad, J. Catal. 213 (2005) 331.
[56] S. Irusta, J. Munera, C. Carrara, E.A. Lombardo, L.M. Cornaglia, Appl. Catal. A Gen. 287 (2005) 147.